FIGURE 5. *Intraoperative photomicrograph (A) and results of computational fluid dynamics analysis (B-H) from case 27. A, intraoperative photomicrograph showing an aneurysm with some thick-walled patches but without atherosclerosis. B through D, contour maps of relative residence time (RRT; B), oscillatory shear index (OSI; C), and time-averaged wall shear stress (WSS; D) from the same viewing angle as in A. Maximum RRT is 6.6 (B, arrow) and is localized at the same point as maximum OSI (0.23) and minimum WSS (0.28 Pa). Snapshots of WSS vector plots captured at end diastole (E) and peak systole (F) showing that there is a whirl-like arrangement of WSS vectors on the surface. Snapshots of the flow field (3-dimensional streamlines) captured at end diastole (G) and peak systole (H) showing that there is a small vortex (G and H, white squares) that is localized at the point with maximum RRT and OSI.*

considered to be fairly small if the vascular geometry is correctly modeled.[16,23] Therefore, we believe that our CFD simulation using patient-derived high-resolution geometries and pulsatile inlet flow rates can reproduce the flow fields and spatial distribution of RRT. However, careful consideration should be taken in quantitative assessment of our CFD results, especially for the possibility of overestimation of WSS owing to numerical simulation under the newtonian fluid and rigid wall conditions.

CONCLUSION

The area with prolonged RRT colocalized with atherosclerotic lesions on the aneurysm wall. Intra-aneurysmal vortex and flow expansion at the bleb were recognized as local flow patterns responsible for the prolongation of RRT. Male sex and prolonged RRT were independent risk factors for atherosclerotic lesions of the intracranial aneurysms.

Disclosures

REFERENCES

1. Wiebers DO, Whisnant JP, Huston J 3rd, et al. Unruptured intracranial aneurysms: natural history, clinical outcome, and risks of surgical and endovascular treatment. *Lancet.* 2003;362(9378):103-110.
2. Morita A, Kirino T, Hashi K, et al. The natural course of unruptured cerebral aneurysms in a Japanese cohort. *N Engl J Med.* 2012;366(26):2474-2482.
3. Cebral JR, Mut F, Raschi M, et al. Aneurysm rupture following treatment with flow-diverting stents: computational hemodynamics analysis of treatment. *AJNR Am J Neuroradiol.* 2011;32(1):27-33.
4. Xiang J, Natarajan SK, Tremmel M, et al. Hemodynamic-morphologic discriminants for intracranial aneurysm rupture. *Stroke.* 2011;42(1):144-152.
5. Karmonik C, Yen C, Grossman RG, Klucznik R, Benndorf G. Intra-aneurysmal flow patterns and wall shear stresses calculated with computational flow dynamics in an anterior communicating artery aneurysm depend on knowledge of patient-specific inflow rates. *Acta Neurochir (Wien).* 2009;151(5):479-485; discussion 485.
6. Cebral JR, Mut F, Weir J, Putman CM. Association of hemodynamic characteristics and cerebral aneurysm rupture. *AJNR Am J Neuroradiol.* 2011;32(2):264-270.
7. Nixon AM, Gunel M, Sumpio BE. The critical role of hemodynamics in the development of cerebral vascular disease. *J Neurosurg.* 2010;112(6):1240-1253.
8. Qian Y, Takao H, Umezu M, Murayama Y. Risk analysis of unruptured aneurysms using computational fluid dynamics technology: preliminary results. *AJNR Am J Neuroradiol.* 2011;32(10):1948-1955.
9. Himburg HA, Grzybowski DM, Hazel AL, LaMack JA, Li XM, Friedman MH. Spatial comparison between wall shear stress measures and porcine arterial endothelial permeability. *Am J Physiol Heart Circ Physiol.* 2004;286(5):H1916-H1922.

10. Hoi Y, Zhou YQ, Zhang X, Henkelman RM, Steinman DA. Correlation between local hemodynamics and lesion distribution in a novel aortic regurgitation murine model of atherosclerosis. *Ann Biomed Eng.* 2011;39(5):1414-1422.
11. Chiu JJ, Chen CN, Lee PL, et al. Analysis of the effect of disturbed flow on monocytic adhesion to endothelial cells. *J Biomech.* 2003;36(12):1883-1895.
12. Omodaka S, Sugiyama S, Inoue T, et al. Local hemodynamics at the rupture point of cerebral aneurysms determined by computational fluid dynamics analysis. *Cerebrovasc Dis.* 2012;34(2):121-129.
13. Shojima M, Oshima M, Takagi K, et al. Magnitude and role of wall shear stress on cerebral aneurysm: computational fluid dynamic study of 20 middle cerebral artery aneurysms. *Stroke.* 2004;35(11):2500-2505.
14. Malek AM, Alper SL, Izumo S. Hemodynamic shear stress and its role in atherosclerosis. *JAMA.* 1999;282(21):2035-2042.
15. Sugiyama SI, Meng H, Funamoto K, et al. Hemodynamic analysis of growing intracranial aneurysms arising from a posterior inferior cerebellar artery. *World Neurosurg.* 2012;78(5):462-468.
16. Cebral JR, Mut F, Weir J, Putman C. Quantitative characterization of the hemodynamic environment in ruptured and unruptured brain aneurysms. *AJNR Am J Neuroradiol.* 2011;32(1):145-151.
17. He X, Ku DN. Pulsatile flow in the human left coronary artery bifurcation: average conditions. *J Biomech Eng.* 1996;118(1):74-82.
18. Zhao M, Amin-Hanjani S, Ruland S, Curcio AP, Ostergren L, Charbel FT. Regional cerebral blood flow using quantitative MR angiography. *AJNR Am J Neuroradiol.* 2007;28(8):1470-1473.
19. Kataoka K, Taneda M, Asai T, Kinoshita A, Ito M, Kuroda R. Structural fragility and inflammatory response of ruptured cerebral aneurysms: a comparative study between ruptured and unruptured cerebral aneurysms. *Stroke.* 1999; 30(7):1396-1401.
20. Kataoka K, Taneda M, Asai T, Yamada Y. Difference in nature of ruptured and unruptured cerebral aneurysms. *Lancet.* 2000;355(9199):203.
21. Steinman DA, Taylor CA. Flow imaging and computing: large artery hemodynamics. *Ann Biomed Eng.* 2005;33(12):1704-1709.
22. Xiang J, Tremmel M, Kolega J, Levy EI, Natarajan SK, Meng H. Newtonian viscosity model could overestimate wall shear stress in intracranial aneurysm domes and underestimate rupture risk. *J Neurointerv Surg.* 2012;4(5):351-357.
23. Steinman DA. Image-based computational fluid dynamics modeling in realistic arterial geometries. *Ann Biomed Eng.* 2002;30(4):483-497.

Supplemental digital content is available for this article. Direct URL citations appear in the printed text and are provided in the HTML and PDF versions of this article on the journal's Web site (www.neurosurgery-online.com).

Original Paper
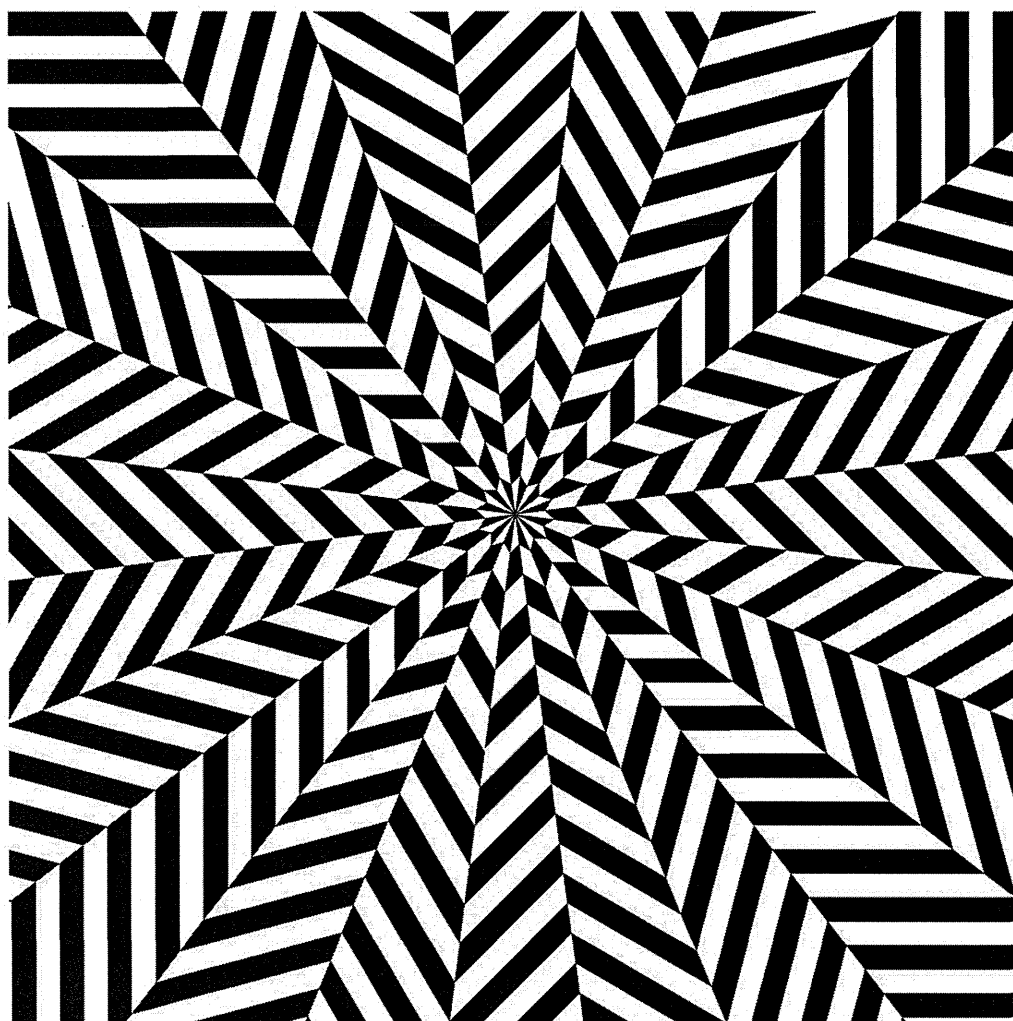
Physiological Evaluation of Visually Induced Motion Sickness Using Independent Component Analysis of Photoplethysmogram

Makoto Abe,[*, #] Makoto Yoshizawa,[**] Norihiro Sugita,[*] Akira Tanaka,[***]
Noriyasu Homma,[**] Tomoyuki Yambe,[†] Shin-ichi Nitta[‡]

Abstract   For continuous evaluation of the effects of visually induced motion sickness (VIMS), we previously proposed a physiological index ρ_{max} that represents the maximum cross-correlation coefficient between blood pressure (BP) and heart rate, the frequency components of which are limited to the Mayer wave-related band. However, ρ_{max} requires continuous BP measurement using a bulky measuring device that is difficult to handle. Thus, we previously proposed an easier method for obtaining ρ_{max} without continuous measurement of BP, which uses only a finger photoplethysmogram (PPG). In this method, independent component analysis (ICA) is used to extract BP-related signals from the PPG signals. However, continuous BP measurement is needed to determine the mixing matrix used in ICA. In order to achieve practical application of the method, this study aim to verify whether each subject's mixing matrix can be estimated based on short-term continuous BP measurement. Being able to do so would mean that ρ_{max} can be obtained from an estimated mixing matrix without continuously measuring BP during an experiment that presents a visual image to a subject. The validity of the proposed method was assessed by experiments performed on 28 subjects watching a swaying video image. From the ex-perimental results, we verified that the proposed method is able to extract independent components related to BP to yield ρ_{max} between heart rate and each independent component used to evaluate the effects of VIMS. This result suggests that the effects of VIMS can be evaluated using short-term continuous BP measurement before the evaluation task.

Keywords : visually induced motion sickness, photoplethysmography, independent component analysis.

Adv Biomed Eng. **2**: pp. 25-31, 2013.

1. Introduction

Nowadays, many people are frequently exposed to various artificial visual images from diverse sources such as video games, movies, web content, and smartphones. Some of these images can cause undesirable effects. One such effect is visually induced motion sickness (VIMS), which causes symptoms related to the autonomic nervous system, such as nausea, vomiting, and dizziness.

Previous studies commonly evaluated VIMS subjectively using questionnaires[1, 2]. However, these methods do not allow estimation of the effects of VIMS as time series data.

To evaluate VIMS objectively and continuously, some researchers have used methods based on cognitive science [3] and motion components of video images [4]. Other researchers have used methods based on physiological parameters such as the heart rate (HR), breathing rate, blood pressure (BP), electrogastrography, and postural stability [5-9]. However, these methods have problems of individual differences and low reproducibility.

To continuously evaluate the effects of VIMS, we previously proposed a physiological index ρ_{max} representing the maximum cross-correlation coefficient between the BP variability and the heart rate variability, the frequency components of which are limited to the Mayer wave-related band [10, 11]. However, ρ_{max} requires continuous BP measurement with an expensive and bulky measuring device. Therefore, only a single subject's data can be obtained from one experiment, and it is difficult to perform an experiment under identical conditions for all subjects.

We have already proposed an easier method for obtaining ρ_{max} using independent component analysis (ICA) to extract BP-related parameters from finger photoplethysmogram (PPG) signals [12-14]. However, BP has to be measured continuously throughout the experiment to determine the mixing matrix used in ICA [12, 13]. Furthermore, the estimated BP-related informa-

tion correlates with BP only under resting conditions[14].

In order to further develop this method for practical application, this study aimed to verify whether each subject's mixing matrix can be estimated based on short-term continuous BP measurement. The novelty and main advantage of the method is that ρ_{max} can be obtained from an estimated mixing matrix without continuously measuring BP during an experiment in which the visual image to be evaluated is presented to the subject. This method would allow collection of long-term and multiple data points at the same time ; for example, when many persons are watching the same movie under the same conditions, because PPG can be measured more easily and economically than BP.

In this paper, we discuss the validity of the proposed method based on experiments performed on 28 subjects watching a swaying video image.

2. Method

2.1 Maximum cross-correlation coefficient

Let $u(i)$ and $v(i)$ ($i=0, 1, 2, \cdots$) denote time series data; i.e., BP variability and heart rate variability (HRV), respectively, sampled for a sampling period of $\Delta t=0.5$ s. They are filtered through a band-pass digital filter with a bandwidth between 0.08 and 0.12 Hz to limit the frequency components to the Mayer wave-related band. At a certain point in time $t=i \cdot \Delta t$ s, a Hamming window with an interval between $t-60$ s and $t+60$ s is applied to $u(i)$ and $v(i)$. A cross-correlation coefficient $\rho_{uv}(\tau)$ for a lag of $\tau=j \cdot \Delta t$ s, $j=\cdots, -1, 0, 1, \cdots$, is calculated as follows:

$$\rho_{uv}(\tau) = \frac{\varphi_{uv}(\tau)}{\sqrt{\varphi_{uu}(0) \cdot \varphi_{vv}(0)}} \quad (1)$$

where $\varphi_{uv}(\tau)$ is a cross-correlation function between $u(i)$ and $v(i)$. and $\varphi_{uu}(\tau)$ and $\varphi_{vv}(\tau)$ are autocorrelation functions of $u(i)$ and $v(i)$, respectively. The maximum cross-correlation coefficient ρ_{max} and its delay τ_{max} are defined as

$$\rho_{max} = \max_{0s \leq \tau \leq 10s} \rho_{uv}(\tau) \quad (2)$$

$$\tau_{max} = \arg \max_{0s \leq \tau \leq 10s} \rho_{uv}(\tau) \quad (3)$$

In the present study, ρ_{max} was successively calculated every 1 s between $t=60$ s (i.e., start time of calculation of ρ_{max}) and $t=T-60$ s (i.e., end time of calculation of ρ_{max}), where T s is the end time of the data obtained from an experiment.

2.2 Independent component analysis (ICA)

ICA is used in our method as follows:

1) Let $x_1(k)$, $x_2(k)$, $\cdots$, $x_m(k)$ be m variables extracted from the PPG signal at the k-th beat. Define feature vector $x(k)$ as $x(k) = [x_1(k), x_2(k), \cdots, x_m(k)]^T$.

2) Let $s_1(k)$, $s_2(k)$, $\cdots$, $s_n(k)$ be n unknown physiological parameters that are independent of one another at the k-th beat. Define parameter vector $s(k)$ as $s(k) = [s_1(k), s_2(k), \cdots, s_n(k)]^T$.

3) Assume that feature vector $x(k)$ is given by a linear combination of $s_1(k)$, $s_2(k)$, $\cdots$, $s_n(k)$ as

follows:

$$x(k) = As(k) \quad (4)$$

where $m \times n$ matrix A represents an unknown constant mixing matrix consisting of coefficients of the linear combination. Let K be the number of beats observed in an experiment. Define $m \times K$ matrix X and $n \times K$ matrix S as $X = [x(1), x(2), \cdots, x(K)]$ and $S = [s(1), s(2), \cdots, s(K)]$, respectively. Thus, matrix X is assumed to be given by S as follows:

$$X = AS \quad (5)$$

4) ICA is applied to estimate mixing matrix A from matrix X. Independent component S can be obtained by

$$S = A^+ X \quad (6)$$

where A^+ is the pseudoinverse matrix of A.

In this study, we used the first fixed point algorithm (fast-ICA) presented by Hyvärinen and Oja to linearly separate S from X [15, 16]. In addition, the number of feature variables m was set to 7.

2.3 Photoplethysmogram (PPG)

A PPG is obtained optically from the volumetric measurement of a blood vessel at the fingers or ears. In general, a PPG sensor consists of a near-infrared LED and photodiode for detecting reflection at the surface of the fingers or ears. The PPG signals can be measured non-invasively, easily, and inexpensively.

Figure 1 shows an example of the PPG signal. This figure shows seven feature variables used in the present study. These are defined for every beat as follows:

1) FFI: foot-to-foot interval of the PPG
2) t_d: interval from the time of maximum value of the PPG to time of minimum value of the PPG
3) $t_{max slope}$: time of maximum slope of the PPG
4) PW_{bias}: minimum value of the PPG
5) PW_{max}: maximum value of the PPG
6) DPW_{max}: value of the PPG at $t_{maxslope}$
7) $NPWA$: area of the PPG normalized by FFI

These parameters may include information on the hemodynamic state, such as BP and vascular compliance. For example, parameter $NPWA$ shows the mean value of the pulsatile component of the arterial blood volume and is a candidate to substitute BP [17]. FFI is used to calculate HR.
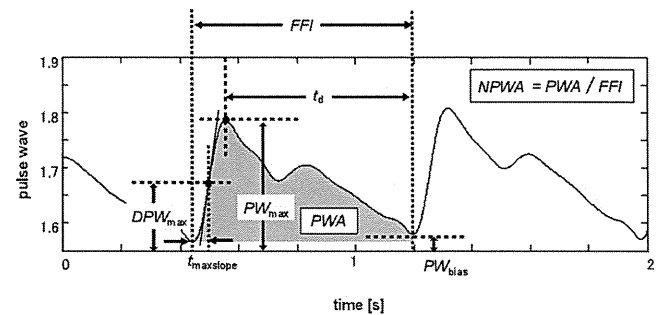

Fig. 1 Definition of feature variables $x_1(k)$, $x_2(k)$, $\cdots$, $x_m(k)$ ($m=7$) and the normalized pulse wave area ($NPWA$).

2.4 Experiment

In this study, 28 healthy subjects (20 males and 8 females, 23.2 ± 3.8 years) participated in an experiment in which they were shown a swaying video image projected by a LCD projector, as presented in **Fig. 2**. The video was filmed by a handheld camera swaying continuously for about 17 min. Thus, the subjects were at an increased risk of VIMS. Before and after watching the video, the subjects watched a still picture of a landscape for 5 min as control. The subject's ECG, continuous BP, and finger PPG were recorded during the experiment. After the second rest, the simulator sickness questionnaire (SSQ) [1] was given to the subject. The total score (*TS*) of the SSQ was calculated to obtain the subjectively evaluated intensity of VIMS.

The experimental protocol was approved by the Internal Review Board of Tohoku University, and informed consent was obtained from all subjects before the experiment.

2.5 Analyses

Based on the observed matrix X obtained from the experimental data, the mixing matrix A, its pseudoinverse A^{+}, and the independent component matrix S were calculated by ICA for each subject. Let n independent component time series IC_l; $l=1, 2, \cdots, n$ as $IC_l = \{s_l(1), s_l(2), \cdots, s_l(K)\}$ with data size K be defined as corresponding to the length of the experiment.

Let time series $\rho_{\max}(BP)$ and $\rho_{\max}(IC_l)$ denote $\rho_{\max}$ between HR obtained from the ECG signal and BP, and $\rho_{\max}$ between HR obtained from the PPG signal and independent component IC_l, respectively.

Let l_{BP}^n denotes the optimal number of l that minimizes the mean square error between $\rho_{\max}(BP)$ and $\rho_{\max}(IC_l)$ as follows:

$$l_{BP}^n = \arg \min_{l=1, \cdots, n} \left(\sqrt{E[\{\rho_{\max}(BP) - \rho_{\max}(IC_l)\}^2]} + \lambda \cdot \sqrt{E[\{\tau_{\max}(BP) - \tau_{\max}(IC_l)\}^2]} \right) \quad (7)$$

where λ denotes the weighting factor of the term related to $\tau_{\max}$ and was determined to be 0.1. This is because $\rho_{\max}$ changes from 0 to 1, while $\tau_{\max}$ goes from 0 to

10. The optimal number n_{opt} of independent components is defined to be from 2 to 6. As previously mentioned, we assume that one of the n-th independent components calculated from seven feature vectors corresponds to information of BP variability. Thus, n_{opt} and l_{BP} are defined as follows:

$$n_{opt} = \arg \min_{n=2, \cdots, 6} (l_{BP}^n) \quad (8)$$

$$l_{BP} = l_{BP}^{n_{opt}} \quad (9)$$

$IC_{l_{BP}}$ denotes the independent component time series closest to BP variability BP, as defined in Eq. (7), based on the data of the first rest phase in the experiment. Let $\rho_{\max}(IC_{l_{BP}})$ denotes $\rho_{\max}$ between HR and $IC_{l_{BP}}$. The number of independent components n was empirically set to 4.

In our previous study [12], A^{+} and $IC_{l_{BP}}$ were calculated from all the experimental data. In the present study, A^{+} and $IC_{l_{BP}}$ were calculated from data of the first rest phase only, for a duration of 5 min. Thereafter, the same A^{+} and $IC_{l_{BP}}$ obtained above were applied to all data measured in the experiment. Thus, we only had to measure BP once before the subjects watched the video image. **Figure 3** shows an example of the analysis. **Figure 3**(a) shows the time-series data of seven feature variables; (b) shows the time-series data of independent components IC_l; $l=1, 2, \cdots, 4$ when n_{opt} is 4; (c) shows $\rho_{\max}(IC_l)$ calculated from four independent components; and (d) shows $\rho_{\max}(BP)$ and $\rho_{\max}(IC_{l_{BP}})$ obtained from l_{BP}, which is calculated from Eqs. (7)-(9). The process for the proposed method is based on this figure.

3. Results

The experimental data of 28 subjects were obtained successfully. **Figures 4**(a) and (b) compare $\rho_{\max}(BP)$ and $\rho_{\max}(IC_{l_{BP}})$ during the first rest phase. Each $\rho_{\max}$ was the value averaged every 30 s for a single subject, and the average $\rho_{\max}$ values of all subjects (168 points) were plotted in these figures. The result of **Fig. 4** shows that $\rho_{\max}(IC_{l_{BP}})$ correlates significantly with $\rho_{\max}(BP)$ for the 28 subjects in the first rest phase of the experiment. This result is consistent with the result of our previous study [14].

Figure 5 shows the results of subjective evaluation based on the SSQ. In general, VIMS causes symptoms such as simulator sickness. Thus, the threshold *TS* that determines whether a subject suffers from VIMS was estimated to be 12.6, which was the median value. All subjects were divided into two groups: sick and well. The sick group consisted of 14 subjects with *TS* higher than 12.6, and the well group consisted of 14 subjects with *TS* lower than 12.6.

Figures 6 and 7 show the changes in $\rho_{\max}(BP)$ and $\rho_{\max}(IC_{l_{BP}})$, respectively, over time. In these figures, $\rho_{\max}$ of the sick and well groups were compared. The shaded areas shown in these figures represent the duration in which a significant difference between the two groups was found by Welch's t-test.

As shown in **Figs. 6 and 7**, $\rho_{\max}(BP)$ and $\rho_{\max}(IC_{l_{BP}})$ of
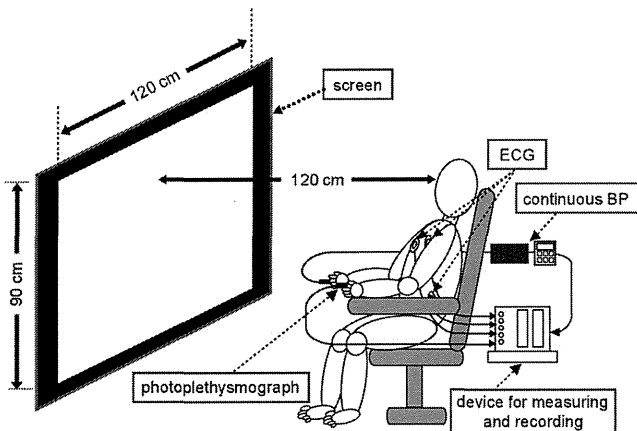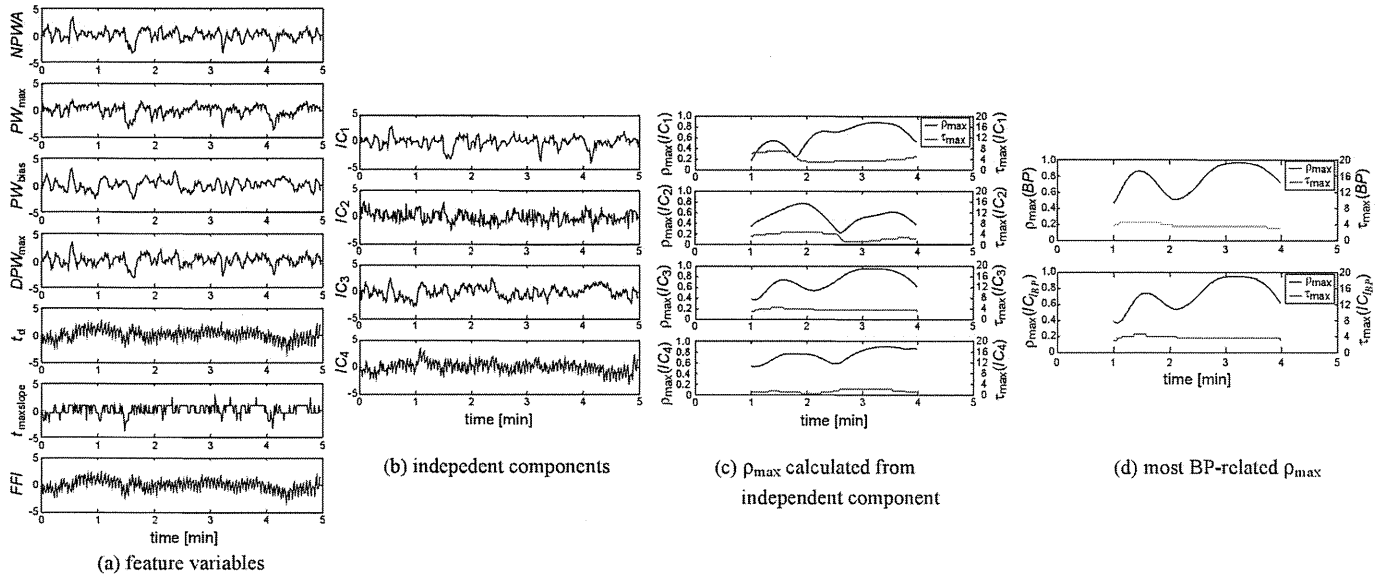

Fig. 2 Experimental setup.

(a) feature variables

(b) indepedent components

(c) ρ_{max} calculated from
independent component

(d) most BP-related ρ_{max}

Fig. 3　An example of ICA for a subject during the experiment.

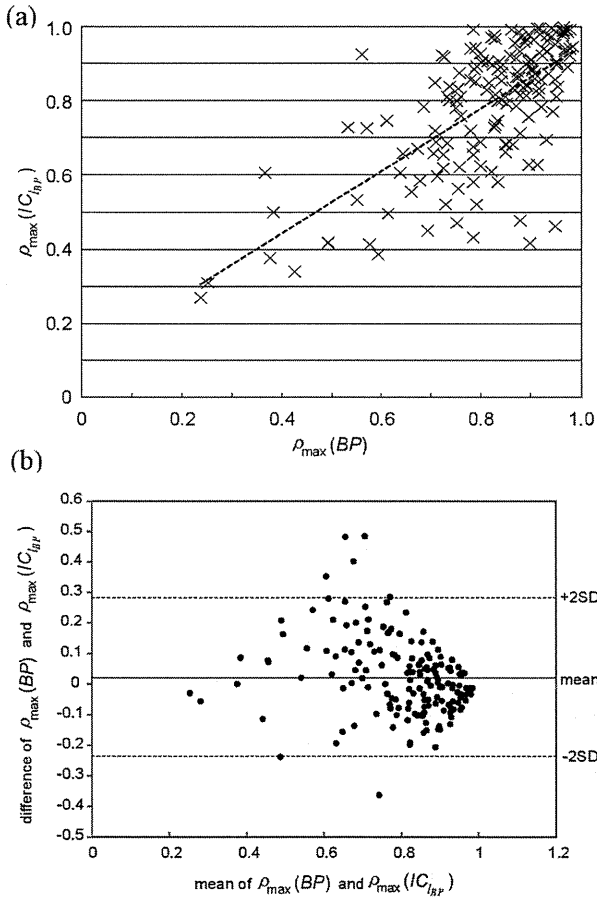**Fig. 4**　(a) Correlation plot between $\rho_{max}(BP)$ and $\rho_{max}(IC_{l_{BP}})$ during the first rest phase. $r=0.69\,(p < 0.01)$. (b) Bland-Altman plot between $\rho_{max}(BP)$ and $\rho_{max}(IC_{l_{BP}})$ during the first rest phase.

the sick group were significantly lower than those of the well group. This result suggests that the decrease in $\rho_{max}(BP)$ or $\rho_{max}(IC_{l_{BP}})$ reflects the effects of VIMS
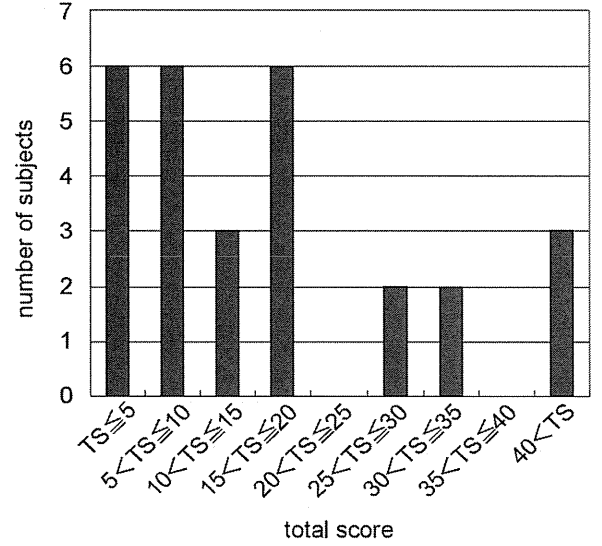

Fig. 5　Subjective evaluation based on total score (TS) of SSQ.

induced by watching the swaying video image. The significant differences between the $\rho_{max}(BP)$ values of the sick and well groups, as shown in **Fig. 6**, imply that the effects of VIMS were especially strong at around 18 min. Similarly, $\rho_{max}(IC_{l_{BP}})$ of the sick group was significantly lower than that of the well group at around 18 min. This result indicates that $\rho_{max}(IC_{l_{BP}})$ calculated using the mixing matrix obtained from the first rest phase is suitable for estimating the effects of VIMS. However, the time showing significant differences between two groups in **Fig. 7** does not correspond precisely to that in **Fig. 6**. The reason for this result should be studied in detail.

Figure 8 shows $\rho_{max}(IC_{l_{BP}})$ obtained from A^+ and $IC_{l_{BP}}$ calculated from all the experimental data by the previous method[12].

A comparison between $\rho_{max}(IC_{l_{BP}})$ obtained by the

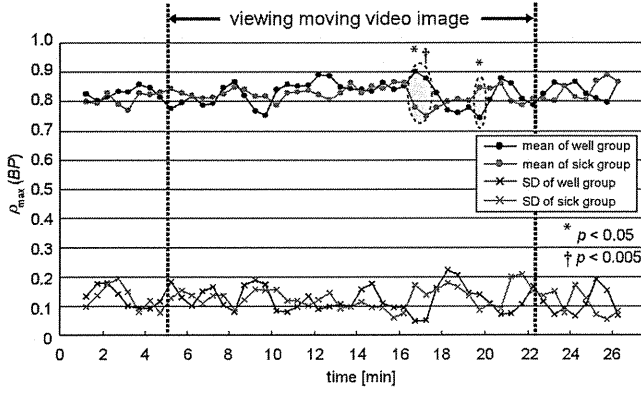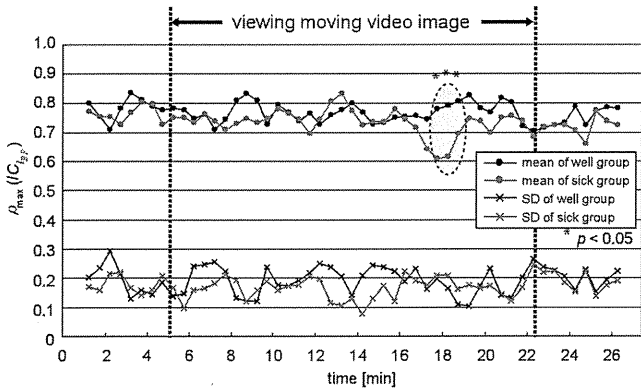**Fig. 6** Comparison of ρ_{max} derived from BP between sick and well groups.

Fig. 7 Comparison of ρ_{max} derived from $IC_{l_{BP}}$ between sick and well groups.
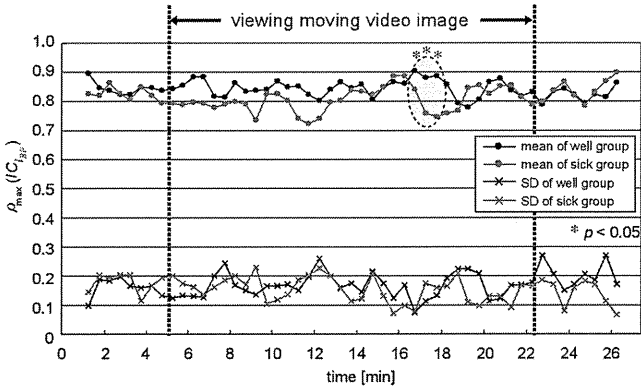

Fig. 8 Comparison of ρ_{max} derived from $IC_{l_{BP}}$ between sick and well groups by the previous method[12].

proposed method in this study and that obtained by the previous method showed that both displayed similar tendencies; that is, $\rho_{max}(IC_{l_{BP}})$ of the sick group was significantly lower than that of the well group at around 18 min. Therefore, the proposed method is superior to the previous method[12] because only short-term continuous BP measurement is required. However, the time showing significant differences in $\rho_{max}(BP)$ was closer to ρ_{max}

$(IC_{l_{BP}})$ obtained by the previous method than to ρ_{max} $(IC_{l_{BP}})$ obtained by the proposed method. This fact indicates that ρ_{max} obtained by the proposed method has scope for improvement.

4. Discussion

The result from **Fig. 4 (a)** shows that $\rho_{max}(IC_{l_{BP}})$ correlates significantly with $\rho_{max}(BP)$ in the rest phase. This result is consistent with the result of our previous study [14]. Thus, reliable feature parameters such as A^{+} and $IC_{l_{BP}}$ were obtained from the 5-min experiment. This finding indicates that once the personal feature parameters are obtained during the first rest phase, there is no need to measure BP continuously during the experiment in which the visual image to be evaluated is presented to the subject. Therefore, many subjects can watch the same movie under the same condition using the proposed method.

In addition, A^{+} and $IC_{l_{BP}}$ calculated from short-term continuous BP measurement in the first rest phase have versatility to the other phases in **Fig. 7**. This result shows that the proposed method has wider applicability than the previous methods[13, 14].

Although the proposed method has great potential, it has several problems that need to be addressed.

In this study, since the subjects watched the swaying video image immediately after the first rest phase, the change in $\rho_{max}(IC_{l_{BP}})$ was similar to the change in ρ_{max} (BP). On the other hand, if a subject's hemodynamics change drastically compared with the first rest phase, A^{+} and $IC_{l_{BP}}$ may be changed. Therefore, we have to examine the reproducibility and individual differences of the proposed method.

Furthermore, since the time showing significant differences between two groups in **Fig. 7** does not correspond precisely to that in **Fig. 6**, $IC_{l_{BP}}$ does not conform exactly to BP variability. In this regard, we should elucidate the physiological mechanisms of independent components such as $IC_{l_{BP}}$.

In addition, we determined the number of feature variables by trial and error in the present study. We should now try to develop a method for choosing the appropriate number of feature variables.

5. Conclusion

To quantify the effect of VIMS, we proposed a new method for extracting BP-related parameter from finger photoplethysmogram using independent component analysis based on short-term continuous measurement of BP before the evaluation task. Experimental results demonstrated that the proposed method is able to extract the independent component related to BP and yield the maximum cross-correlation coefficient ρ_{max} between heart rate and the independent component used to evaluate the effects of VIMS.

In the future, we should develop a method for determining the mixing matrix with the photoplethysmogram using other mathematical theories or calculation

algorithms for independent component analysis. In addition, elucidating the physiological mechanisms of independent components other than the BP-related component is important.

References

1. Kennedy RS, Lane NE, Berbaum KS, Lilienthal MG: Simulator sickness questionnaire: An enhanced method for quantifying simulator sickness. Int J Aviat Psychol. **3** (3), pp. 203–220, 1993.

2. Jones MB, Kennedy RS. Stanney KM : Toward systematic control of cybersickness. Presence, Teleoperators Virtual Environ. **13**(5), pp. 589–600, 2004.

3. Golding JF, Doolan K, Acharya A, Tribak M, Gresty MA: Cognitive cues and visually induced motion sickness. Aviat Space Environ Med. **83**(5), pp. 477–482, 2012.

4. Keshavarz B, Hecht H: Axis rotation and visually induced motion sickness: the role of combined roll, pitch, and yaw motion. Aviat Space Environ Med. **82**(11), pp. 1023–1029, 2011.

5. Graybiel A, Lackner JR: Evaluation of relationship between motion sickness symptomatology and blood pressure, heart rate, and body temperature. Aviat Space Environ Med. **51**, pp. 211–214, 1980.

6. Kim YY, Kim EN, Jae PM, Park KS, Ko HD, Kim HT: The application of biosignal feedback for reducing cybersickness from exposure to a virtual environment. Presence, Teleoperators Virtual Environ. **17**(1), pp. 1–16, 2008.

7. Nichols S, Cobb S, Wilson JR: Health and safety implications of virtual environments: Measurement issues. Presence, Teleoperators Virtual Environ. **6**, pp. 667–675. 1997.

8. Palmisano S, Allison RS, Kim J, Bonato F: Simulated viewpoint jitter shakes sensory conflict accounts of vection. Seeing Perceiving. **24**(2), pp. 173–200, 2011.

9. Ohsuga M, Shimono F, Genno H: Assessment of phasic work stress using autonomic indices. Int J Psychophysiol. **40**(3), pp. 211–220, 2001.

10. Sugita N, Yoshizawa M, Abe M, Tanaka A, Watanabe T, Chiba S, Yambe T, Nitta S: Evaluation of adaptation to visually induced motion sickness based on the maximum cross-correlation between pulse transmission time and heart rate. J Neuroeng Rehabil. **4**, pp. 35 (online journal; http://www.jneuroengrehab.com/content/4/1/35), 2007.

11. Sugita N, Yoshizawa M. Tanaka A, Abe K, Chiba S, Yambe T, Nitta S: Quantitative evaluation of effects of visually-induced motion sickness based on causal coherence functions between blood pressure and heart rate. Displays. **29**, pp. 167–175, 2008.

12. Abe M, Yoshizawa M, Sugita N, Tanaka A, Chiba S, Yambe T. Nitta S: A method for evaluating effects of visually-induced motion sickness using ICA for photoplethysmography. Proc of 30th Annual International Conference of the IEEE Engineering in Medicine and Biology Society. Vancouver, pp. 4591–4594, 2008.

13. Abe M, Yoshizawa M, Sugita N, Tanaka A, Chiba S, Yambe T, Nitta S: Estimation of blood pressure variability using independent component analysis of photoplethysmographic signal. Proc of 31st Annual International Conference of the IEEE Engineering in Medicine and Biology Society. Minneapolis, pp. 2498–2501, 2009.

14. Abe M, Yoshizawa M, Sugita N, Tanaka A, Homma N, Yambe T, Nitta S: Estimation of baroreflex function using independent component analysis of photoplethysmography (in Japanese). IEEJ Trans EIS. **131** (9), pp. 1540–1546, 2011.

15. Hyvärinen A: Fast and robust fixed-point algorithms for independent component analysis. IEEE Trans Neural Networks. **10**(3), pp. 626–634, 1999.

16. Hyvärinen A, Oja E: A fast fixed-point algorithm for independent component analysis. Neural Comput. **9**, pp. 1483–1492. 1997.

17. Abe M, Yoshizawa M, Sugita N, Tanaka A, Chiba S, Yambe T, Nitta S: Physiological evaluation of effects of visually-induced motion sickness using finger photoplethysmography. Proc of SICE-ICASE International Joint Conference, Busan, pp. 2340–2343, 2006.

Makoto ABE

He received the B.S., M.S. and Ph.D. degrees in Electrical and Communication Engineering from Tohoku University in 2004, 2006 and 2009, respectively. He was a Postdoctoral Fellow from 2009 to 2010 in Cyberscience Center, Tohoku University. Since 2011, he has been an Assistant Professor in Graduate School of Engineering, Tohoku University. He engages in evaluation of effects of visual stimulation on humans and development of a detection algorithm of fatal arrhythmias for the implantable cardioverter-defibrillator. He has been a member of the society of IEEE and the Japanese Society for Medical and Biological Engineering.

Makoto YOSHIZAWA

He received the B.S., M.S. and Ph.D. degrees in Electrical and Communication Engineering from Tohoku University in 1978, 1980 and 1983, respectively. He was a Research Associate from 1983 to 1991 in the same department. Since 1991 to 1994, he was an Associate Professor in Toyohashi University of Technology, Toyohashi, Japan. In 1994, he returned to Tohoku University. He became a Visiting Scientist, Research Institute of Medicine, Johns Hopkins University, Baltimore and Baylor College of Medicine, Houston, U.S.A. in 1999. Since 2001, he has been a Professor in the Research Division on Advanced Information Technology, Information Synergy Center (currently, Cyberscience Center), Tohoku University. He engages in application of virtual reality to medicine, intelligent control of artificial hearts, assessment of effects of visual stimulation on humans and tele-healthcare. He was a member of AdCom of IEEE EMBS From 2009 to 2011. He has been a member of Editorial Committee and a councilor of Journal of the Japanese Society for Medical and Biological Engineering.

Norihiro SUGITA

He received the B.S., M.S. and Ph.D. degrees in engineering from Tohoku University, Sendai, Japan, in 1998, 2001 and 2004, respectively. He was a COE Research Fellow from 2004 to 2006 and an Assistant Professor from 2006 to 2010 in the Department of Electrical and Communication Engineering, Graduate School of Engineering, Tohoku University. He is currently an Associate Professor in the Department of Management Science and Technology, Graduate School of Engineering, Tohoku University. His research interests include application of virtual reality to medicine, assessment of effects of visual stimulation on humans and tele-healthcare. He is a member of Japanese Telemedicine and Telecare Association and the Society of Instrument and Control Engineers of Japan.

Akira TANAKA

He received the Ph.D. degrees in Engineering from Tohoku University in 1998. From 1998 to 2000, he was a Research Fellow of the Japan Society for the Promotion of Science. From 2001 to 2004, he was a Research Associate in the Graduate School of Engineering, Tohoku University. Since 2004, he has been an Associate Professor in Faculty of Symbiotic Systems Science, Fukushima University. His research interests include cardiovascular signal processing and analysis of physiological reaction. He is a member of the society of IEEE and Japanese Society for Artificial Organs.

Noriyasu HOMMA

He received the B.S., M.S. and Ph.D. degrees in electrical and communication engineering from Tohoku University in 1990, 1992 and 1995, respectively. From 1995 to 1998, he was a lecturer at the Tohoku University, Japan. He is currently an associate professor of the Cyberscience Center at the Tohoku University. From 2000 to 2001, he was a visiting professor at the Intelligent Systems Research Laboratory, University of Saskatchewan, Canada. His current research interests include neural networks, complex and chaotic systems, soft-computing, cognitive sciences, medical systems and brain sciences. He has been an associate editor of Journal of Intelligent & Fuzzy Systems since 2006 and a member of NNTC of IEEE Computational Intelligence Society since 2007.

Tomoyuki YAMBE

He received the M.D. and Ph.D. degrees in Medical Science from Tohoku University, Sendai, Japan, in 1986 and 1989, respectively. He was a Research Associate from 1992 at the Division of Medical engineering and Clinical investigation and Department of Medical Engineering and Cardiology, Institute of Development, Aging and Cancer, Tohoku University. He has been a Professor in the some department from 2004. He engages in artificial heart, autonomic nervous system analysis and telemedicine. He is a member of Japanese Society for Artificial Organs, the Japanese Society for Medical and Biological Engineering, and Japanese Society of Neurovegetative Research.

Shin-ichi NITTA

He graduated from Tohoku University School of Medicine in 1966. He was a Researcher at the Texas Heart Institute, Houston, USA in 1974. He was an Assistant professor of Tohoku University at Institute of Development, Aging and Cancer in 1981. He was Professor of Tohoku University at Institute of Development, Aging and Cancer in 1996. In 1996 he was a Concurrent professor at Tokyo Institute of Technology. In 2003 he was a Professor of Tohoku University of Division of Medical engineering and Clinical investigation at Institute of Development, Aging and Cancer. He is an emeritus professor of Tohoku University from 2010.

INVERSE PROBLEMS IN CARDIOVASCULAR MATHEMATICS

Reproduction of pressure field in ultrasonic-measurement-integrated simulation of blood flow

Kenichi Funamoto[*,†] and Toshiyuki Hayase

Institute of Fluid Science, Tohoku University, 2-1-1 Katahira, Aoba-ku, Sendai 980-8577, Japan

SUMMARY

Ultrasonic-measurement-integrated (UMI) simulation of blood flow is used to analyze the velocity and pressure fields by applying feedback signals of artificial body forces based on differences of Doppler velocities between ultrasonic measurement and numerical simulation. Previous studies have revealed that UMI simulation accurately reproduces the velocity field of a target blood flow, but that the reproducibility of the pressure field is not necessarily satisfactory. In the present study, the reproduction of the pressure field by UMI simulation was investigated. The effect of feedback on the pressure field was first examined by theoretical analysis, and a pressure compensation method was devised. When the divergence of the feedback force vector was not zero, it influenced the pressure field in the UMI simulation while improving the computational accuracy of the velocity field. Hence, the correct pressure was estimated by adding pressure compensation to remove the deteriorating effect of the feedback. A numerical experiment was conducted dealing with the reproduction of a synthetic three-dimensional steady flow in a thoracic aneurysm to validate results of the theoretical analysis and the proposed pressure compensation method. The ability of the UMI simulation to reproduce the pressure field deteriorated with a large feedback gain. However, by properly compensating the effects of the feedback signals on the pressure, the error in the pressure field was reduced, exhibiting improvement of the computational accuracy. It is thus concluded that the UMI simulation with pressure compensation allows for the reproduction of both velocity and pressure fields of blood flow. Copyright © 2012 John Wiley & Sons, Ltd.

1. INTRODUCTION

Circulatory diseases such as heart disease and cerebrovascular disease are major causes of death. *In vivo* and *in vitro* experiments and numerical simulations of blood flow have been extensively carried out, indicating the relationships between diseases and hemodynamics [1, 2]. Blood flow information acquired by medical imaging techniques, such as ultrasonic measurement, magnetic resonance imaging (MRI) and computed tomography (CT), or directly measured by a catheter, sphygmomanometer or electrocardiogram is limited. On the other hand, blood flow simulation provides detailed information on three-dimensional unsteady hemodynamics including wall shear stress and pressure distributions. However, as it is inherently difficult to correctly specify the boundary and initial conditions, the computational results may differ from the real blood flow field data [3,4]. Several methods have been proposed for flow simulation using defective boundary conditions, in which only flow rates are known [5,6]. However, their efficiency for blood flow in a complicated

---

*Correspondence to: Kenichi Funamoto, Institute of Fluid Science, Tohoku University, 2-1-1 Katahira, Aoba-ku, Sendai 980-8577, Japan.

†E-mail: funamoto@reynolds.ifs.tohoku.ac.jp

vessel configuration remains to be investigated. Other factors, such as assumption of a rigid vessel wall, and uncertainties in vessel geometry, physical properties, and the model of the blood rheology, can also introduce errors into the computation. Consequently, at present, the diagnosis of circulatory diseases depends on empirical knowledge with limited measurement data. An innovative technique for accurate and detailed reproduction of blood flow field in a blood vessel is needed to realize more accurate and reliable diagnoses.

Various methodologies have been developed to computationally reproduce a flow field by integrating measurement and computation to overcome individual disadvantages. These methods include a method using proper orthogonal decomposition [7,8], data assimilation based on Tichonov regularization [9], least-squares finite element methods [10, 11], the Kalman filter [12], variational methods [13, 14], and measurement-integrated (MI) simulation [15–18]. Data assimilation based on four-dimensional variation is widely used, especially in numerical weather forecasting [14]. However, it requires huge computational resources to repeatedly solve flow dynamics and its adjoint, and therefore, is not suitable for application to problems of real-time flow reproduction. In contrast, the Kalman filter and MI simulation are rather simple methods sequentially comparing the computational result with the corresponding measurement data and directly feeding back the differences to the numerical simulation. Compared with the Kalman filter, which usually employs a low-dimensional linear model, the MI simulation, which uses computational fluid dynamics as a mathematical model, can provide a solution with high accuracy once a convergent result is obtained although there is no systematic design method of the feedback signal. The authors have applied MI simulation to blood flow analysis by integrating medical measurement (ultrasonic measurement or phase-contrast MRI) and numerical simulation [19,20]. With ultrasonic-measurement-integrated (UMI) simulation, the blood flow field is analyzed by applying artificial body forces proportional to the differences between the measured and computed Doppler velocities of the blood flow. Figure 1 shows a block diagram of the UMI simulation. Note that a 'Pressure compensation' block is newly added in this paper as explained in the following section. In our previous studies, a two-dimensional UMI simulation using real ultrasound color Doppler images was conducted [19]. The transient and steady characteristics of UMI simulation and the efficiency of feedback to reproduce unsteady three-dimensional hemodynamics were investigated by numerical experiments [21–23]. Those studies revealed that the UMI simulation improved computational accuracy in comparison with the ordinary simulation, making the computational velocity vector field approach that of a model solution of real blood flow. However, the reproducibility of the pressure field was not necessarily satisfactory [21,24].

In this study, reproduction of the pressure field by UMI simulation was investigated. In the second section of this paper, the effect of feedback based on Doppler velocity on the pressure field is first examined by theoretical analysis, and a pressure compensation method is derived. In the third section, results of the theoretical analysis and the proposed pressure compensation method are validated by a numerical experiment dealing with a synthetic three-dimensional steady flow in a thoracic aneurysm.
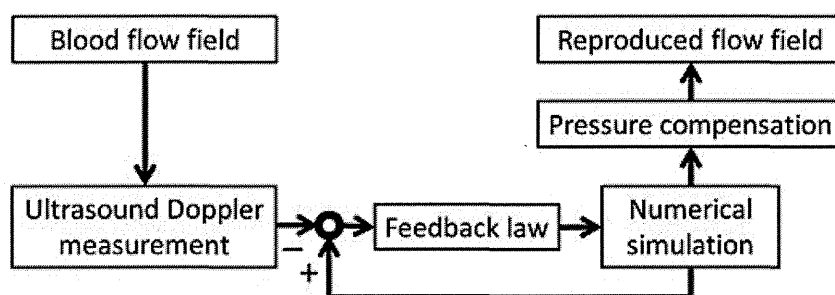

Figure 1. Block diagram of the UMI simulation.

2. THEORETICAL ANALYSIS

The effect of the feedback signal on the pressure field in the UMI simulation is clarified by theoretical analysis, and a pressure compensation method is developed.

2.1. Effect of feedback signals on the pressure field

The governing equations of the UMI simulation of blood flow in a blood vessel are the Navier–Stokes equations and the equation of continuity.

$$\rho \left(\frac{\partial \mathbf{u}}{\partial t} + (\mathbf{u} \cdot \nabla) \, \mathbf{u} \right) = \mu \Delta \mathbf{u} - \nabla p + \mathbf{f}, \tag{1}$$

$$\nabla \cdot \mathbf{u} = 0, \tag{2}$$

where $\mathbf{u} = (u, v, w)$ is the velocity vector, p is the pressure, ρ is the density, μ is the viscosity, t is the time, and $\mathbf{f} = (f_x, f_y, f_z)$ is the external force term corresponding to the feedback signal. By substituting Equation (2) into the divergence of Equation (1), the pressure equation is derived as follows:

$$\Delta p = -\nabla \cdot \rho (\mathbf{u} \cdot \nabla) \, \mathbf{u} + \nabla \cdot \mathbf{f}. \tag{3}$$

Equations (1) and (3) are employed as the governing equations in the following analysis.

Regarding the boundary conditions, correct velocity profiles are assumed to be unknown, and a uniform or parabolic parallel profile with a known flow volume and free flow condition are specified at the upstream and downstream boundaries, respectively. The initial flow condition is an arbitrary flow field.

The feedback signal, $\mathbf{f}$, in Equation (1) is an artificial body force, which is proportional to the difference between the computed and measured Doppler velocities in the feedback domain defined in the computational domain:

$$\mathbf{f} = -K_v^* \frac{\Phi_d (\mathbf{u} - \mathbf{u}_s)}{U} \left(\frac{\rho U^2}{L} \right), \tag{4}$$

where K_v^* is the feedback gain (nondimensional), U is the characteristic velocity, L is the characteristic length, and $\mathbf{u}_s$ is the velocity vector of the real blood flow. Φ_d ($d = 1, 2, 3$) is a projection function of a three-dimensional vector to the d-dimensional subspace [21]. The projection of the three-dimensional velocity vector in the direction of the ultrasonic beam in the UMI simulation corresponds to the case of $d = 1$, and $\Phi_1(\mathbf{u})$ and $\Phi_1(\mathbf{u}_s)$ correspond to computed and measured Doppler velocities, respectively. Here, measurement errors, such as noise, contained in ultrasonic Doppler measurement are ignored for simplicity. Note that, in our previous study [23], the effects of major measurement errors on the computational accuracy of the UMI simulation were investigated, and methods to compensate those effects were proposed. The special case with $K_v^* = 0$ corresponds to the ordinary numerical simulation without feedback.

Previous studies [21–23] have revealed that with a proper application of feedback, the computational velocity field approaches the real velocity field of the blood flow. Generally, because a velocity field has a unique pressure field, it was expected that the computational pressure field would concurrently approach the real pressure field. However, the reproducibility of pressure field was not necessarily satisfactory.

The pressure field by the UMI simulation is discussed in the following. The velocity field, $\mathbf{u}_s$, and the pressure field, p_s, of a real blood flow satisfy governing Equations (1) and (3) without the external force term, $\mathbf{f}$, with the upstream and downstream boundary conditions of the correct velocity profiles and with the initial condition of the correct velocity vector field at the first time step:

$$\rho \left(\frac{\partial \mathbf{u}_s}{\partial t} + (\mathbf{u}_s \cdot \nabla) \, \mathbf{u}_s \right) = \mu \Delta \mathbf{u}_s - \nabla p_s, \tag{5}$$

$$\Delta p_s = -\nabla \cdot \rho (\mathbf{u}_s \cdot \nabla) \, \mathbf{u}_s. \tag{6}$$

In the UMI simulation, incorrect specification of boundary conditions introduces error to the computational result as compared with the real blood flow, but the feedback based on Doppler velocity works to reduce the error in the velocity vector field in the feedback domain. Therefore, in the equation derived from the subtraction of Equation (6) from Equation (3), the velocity vector, **u**, is approximately equal to the real velocity vector, **u**$_s$, and the following equation is approximately satisfied in the feedback domain:

$$\Delta p = \Delta p_s + \nabla \cdot \mathbf{f}. \tag{7}$$

This equation implies that the pressure field, p, of the UMI simulation becomes different from the real pressure field, p_s, because of the effect of feedback in the case that the divergence of the feedback force vector is not zero.

2.2. Pressure compensation method

A pressure compensation method for the UMI simulation is introduced. The pressure compensation is applied after the convergent results of velocity and pressure are obtained (see Figure 1). The correct pressure field, p_s, is expressed as the summation of the computational result, p, and the compensation term, p_f.

$$p_s = p + p_f. \tag{8}$$

With Equation (7) and Equation (8) operated by Laplacian operator, the following equation is obtained.

$$\Delta p_f = -\nabla \cdot \mathbf{f}. \tag{9}$$

The pressure compensation, p_f, is calculated from Equation (9) by setting zero value at the boundaries of the computation domain. In the case that the blood flow is considered to be parallel flow such as the one in a straight blood vessel, pressure is constant over the cross-section perpendicular to the flow. In addition, if the flow rate in the UMI simulation is identical to that of the real flow, the pressure differences between upstream and downstream boundaries are the same between the cases. Consequently, the boundary conditions of the pressure equations for p and p_s can be considered to be the same. Because $p_f = p_s - p$ from Equation (8), the value of p_f should be zero at the upstream and downstream boundaries. By substituting the pressure compensation, p_f, into Equation (8), an estimated value, p_s', of the correct pressure is obtained.

The proposed pressure compensation method is equivalent to a modification of the UMI simulation retaining only the divergence-free part of the feedback signal, $\mathbf{f}_{div}$. The feedback signal, $\mathbf{f}$, can be decomposed to an irrotational part, $\mathbf{f}_{irr}$, and a divergence-free part, based on Helmholtz decomposition [25]. Pressure compensation, p_f, obtained from Equation (9) determines the irrotational part of the feedback signal as $\mathbf{f}_{irr} = -\nabla p_f$, which does not contribute to improvement of the computational accuracy of the velocity field, but deteriorates that of the pressure field.

2.3. Discretization

Outlines of discretization of the governing equations of the UMI simulation, including the pressure compensation equation, are described in this section. The above-mentioned governing equations are discretized by means of the finite volume method and are solved with the SIMPLER method [26]. The concrete notations of the parameters in the following equations, and supplementary pressure correction equations and velocity correction procedure in the SIMPLER method, are explained in [26].

The x-directional momentum equation in Navier–Stokes equations of Equation (1):

$$B_p u_{i,j,k} = \sum B_{nb} u_{nb} + S_{i,j,k} + A_i(p_{i-1,j,k} - p_{i,j,k}) + \Delta V_{i,j,k} f_{x_{i,j,k}}, \tag{10}$$

where Bs are the elements of the matrix consisting of all of the diffusive terms and a part of the convective terms in the discretized Navier–Stokes equation, and $(\sum B_{nb} u_{nb})$ is the summation of

the values at six adjacent nodes in the three-dimensional computation. The second term, $S_{i,j,k}$, on the right side is the source term, which consists of a part of the convective terms and a part of the time-derivative term. The third term is the pressure gradient term in which A_i is the cross-sectional area of the control volume, and the last term is the feedback term in which $\Delta V_{i,j,k}$ is the volume of the cell. Subscript p denotes the position where $u(i,\ j,\ k)$ is defined, and nb means adjacent nodes. Equations for y-directional and z-directional momentums are analogous to that in Equation (10).

The pressure equation of Equation (3):

$$C_P\, p_{i,j,k} = \sum C_{nb} p_{nb} + S_{pi,j,k} + S_{fi,j,k},\tag{11}$$

where Cs are the elements of the matrix derived from discretization of the pressure equation, $S_{pi,j,k}$ is the source term derived from discretization of the first term on the right side of Equation (3), and $S_{fi,j,k}$ is the source term because of the feedback. Subscript P denotes the position where $p(i,\ j,\ k)$ is defined. The source term because of the feedback, $S_{fi,j,k}$, is denoted in the following equation:

$$S_{f_{i,j,k}} = \frac{\rho}{B_p}[(f_{x\,i,j,k} - f_{x\,i+1,j,k})A_i + (f_{y\,i,j,k} - f_{y\,i,j+1,k})\,A_j + (f_{z\,i,j,k} - f_{z\,i,j,k+1})A_k],\tag{12}$$

where A_i, A_j, and A_k are the cross-sectional areas of the control volume facing each direction.

Pressure compensation for feedback of Equation (9):

Equation (9) is also expressed in a way similar to the pressure equation

$$C_p\, p_{f_{i,j,k}} = \sum C_{nb} p_{f_{nb}} - S_{f_{i,j,k}},\tag{13}$$

where coefficients C_p and C_{nb}, and the source term $S_{fi,j,k}$ are identical with those in Equations (11) and (12).

3. VALIDATION WITH NUMERICAL EXPERIMENT

Results of the theoretical analysis and the proposed pressure compensation method are validated by a numerical experiment dealing with a synthetic three-dimensional steady flow in a thoracic aneurysm. Ultrasonic measurement provides the Doppler velocity necessary for the feedback in UMI simulation, but it does not provide other information necessary for evaluating the UMI simulation such as three-dimensional velocity vectors or pressure field. Hence, we do not use real measurement data for the reference data. Instead, we use a numerical solution for a synthetic steady flow with realistic upstream and downstream velocity boundary conditions called 'standard solution' as a model of real blood flow to perform the numerical experiment. The boundary conditions of the standard solution are determined from a preliminary simulation of blood flow in a whole aorta including an aneurysm. Reproduction of the standard solution by the UMI simulations with/without the pressure compensation and the ordinary numerical simulation without feedback are investigated. The numerical simulations conducted in this section are summarized in Table I.

Table I. Classification of preliminary simulation (PS), standard solution (SS), UMI simulation (UMIS), and ordinary simulation (OS).

Name	Solver	Domain	Grid	Boundary velocity	Feedback	Note
PS	FLUENT	Whole aorta Figure 2(a)	Hexahedral 142,417	Uniform inlet Free stream outlet	N/A	Boundary velocity for SS was obtained.
SS	Original (SIMPLER)	Aneurysm Figure 2(b)	Orthogonal $40 \times 34 \times 49$	Specified velocity inlet & outlet	N/A	Model of real flow
UMIS	Original (SIMPLER)	Aneurysm Figure 2(b)	Orthogonal $40 \times 34 \times 49$	Uniform inlet Free stream outlet	Applied	Measurement data was was generated by SS.
OS	Original (SIMPLER)	Aneurysm Figure 2(b)	Orthogonal $40 \times 34 \times 49$	Uniform inlet Free stream outlet	N/A	

3.1. Methods

A numerical experiment was conducted to investigate the computational accuracy of the pressure field by the UMI simulation and to examine the efficiency of the proposed pressure compensation method. The objective was a steady flow in a thoracic aneurysm, which was the same as in a previous study [22]. A steady numerical solution with realistic boundary conditions was first defined as the standard solution. The boundary conditions of the standard solution were determined from a preliminary simulation of blood flow in a whole aorta including the aneurysm. Although generation of synthetic measurement data for validation of new algorithms has been investigated [27,28], the computational three-dimensional velocity vectors were simply projected in the direction of the ultrasonic beam without consideration of measurement errors to obtain the Doppler velocity of the standard solution. Then, with inaccurate boundary conditions but with the correct flow volume, UMI simulation and an ordinary simulation without feedback were performed. In the UMI simulation, Doppler velocities of the standard solution were used for feedback. After the convergent results of velocity and pressure were obtained, the pressure compensation was applied to the pressure field (see Figure 1).

A preliminary simulation for a whole aorta was first performed. The configuration of the whole aorta from the ascending aorta to the abdominal aorta, including an aneurysm in the descending aorta, was reconstructed, as shown in Figure 2(a), by accumulating X-ray CT images (Aquilion 16, Toshiba, Tokyo, Japan) of a 76-year-old female patient with commercial three-dimensional reconstruction software (Mimics 7.3, Materialise, Leuven, Belgium) [22]. A preliminary simulation of a steady blood flow in the whole aorta (Figure 2(a)) was carried out by using commercial computational fluid dynamics software (FLUENT 6.1.22, Fluent, Inc., Lebanon, NH). The computational grid used in the preliminary FLUENT simulation consisted of 142,417 hexahedral elements. Pressure–velocity coupling was accomplished by the SIMPLE method, and spatial discretization schemes were employed as follows: a Green-Gauss cell-based scheme for gradient; a standard scheme for pressure; and a first-order upwind for momentum. Uniform velocity was applied at the inlet boundary so that the average flow rate became 8.65×10^{-5} m^3/s, and a
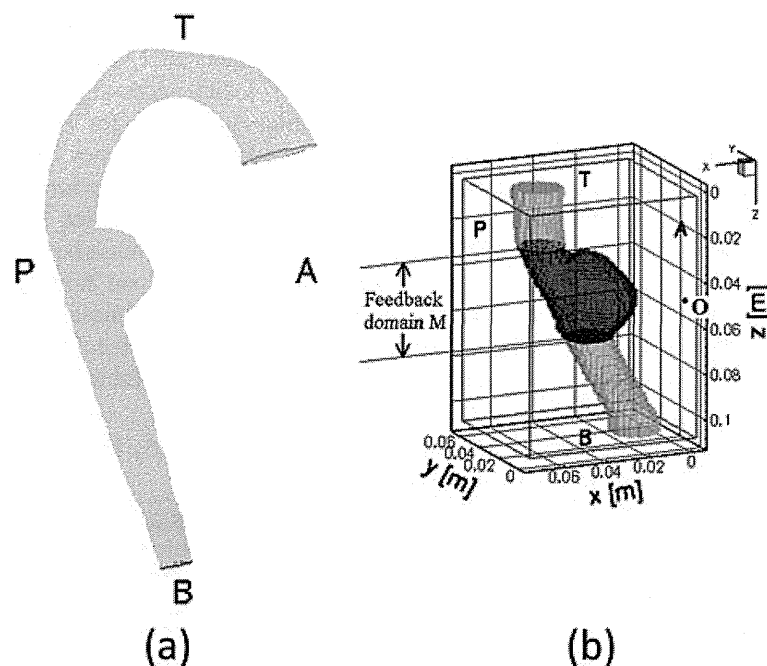

Figure 2. Computational grids for (a) a preliminary simulation of a steady flow in the whole aorta with an aneurysm in the descending aorta by using FLUENT, and for (b) the other simulations of the flow in the partial domain including the aneurysm with a feedback domain (dark gray zone) and a probe position at O.

free-flow condition was applied at the downstream boundary. A no-slip condition was set on the wall. The convergence criterion in the numerical simulation was set at 1×10^{-4} for momentum and continuity equations.

In the following computations for the standard solution, the UMI simulation, and the ordinary simulation, the computational domain was limited to the vicinity of the thoracic aneurysm, as shown in Figure 2(b). A computational grid system was generated by introducing a staggered grid system of $40 \times 34 \times 49$ grid points in x, y, and z directions, compromising reproducibility of vessel configuration and computational load. The grid interval dz in the z direction was set at 2.00×10^{-3} m, which was the same as the slice interval of the X-ray CT, and those in the other directions were determined to be $dx = dy = 1.78 \times 10^{-3}$ m. The equivalent diameter of the blood vessel, D, at the upstream boundary calculated by averaging x-directional and y-directional maximum lengths of the cross-section of the blood vessel at the upstream boundary was 23.47×10^{-3} m. Flow rate was set at 8.65×10^{-5} m³/s (same as the preliminary simulation), and the average flow velocity at the upstream boundary, U, was 2.00×10^{-1} m/s. The density, ρ, and viscosity, μ, of the blood were assumed to be 1.00×10^3 kg/m³ and 4.00×10^{-3} Pa·s, respectively. All the variables were nondimensionalized with the equivalent diameter of the blood vessel, D, as the characteristic length, L, the average flow velocity as the characteristic velocity, U, and the density of blood, ρ, as the characteristic density. The Reynolds number of the steady flow was 1174. From here on, the same symbols are used for both dimensional and nondimensional values because it does not cause any confusion.

In the computation of the standard solution, velocity profiles at the upstream and downstream boundaries were determined as those on the corresponding cross-sections of the preliminary simulation. In the UMI simulation and the ordinary simulation, a uniform parallel flow was applied at the upstream boundary, and the free flow condition was set at the downstream boundary.

Because the computational result converges to the target flow with the aid of the feedback process, unsteady flow computation is required for the UMI simulation even for the present steady target flow. Time-dependent computation was performed for all cases. The computational time increment was set as $\Delta t = 0.01(1.17 \times 10^{-3}$ s) [22].

In UMI simulation, considering the acquisition of Doppler velocities in the three-dimensional domain by transesophageal ultrasonography, the ultrasound probe or the origin of ultrasonic beam was set at O$[(x, y, z) = (0.008, 0.023, 2.045)((0.000$ m, 0.001 m, 0.048 m))], which was located at the same height as the aneurysm, as shown in Figure 2(b). The Doppler beam direction was along a line from the origin of ultrasonic beam to each computational gird point. Blood flow in the whole aneurysmal domain M$[1.193 \leqslant z \leqslant 2.897(0.028$ m $\leqslant z \leqslant 0.068$ m), shown by a dark gray zone in Figure 2(b)], including the parent blood vessel, was assumed to be measured. Domain M was defined as the feedback domain, and at all the grid points in the fluid region of domain M, feedback signals were added to the UMI simulation based on the differences of Doppler velocities between the simulation and the standard solution.

In the computation of the standard solution, the UMI simulation and the ordinary simulation, the governing equations were discretized by the finite volume method and were solved with an original program based on the SIMPLER method [26, 29] as described in the previous section. The convective terms were discretized with the reformulated QUICK scheme [30], and the time derivative terms were discretized with the first Euler implicit scheme. Linear algebraic equations were solved using the modified strongly implicit (MSI) scheme [31]. The convergence criterion in the numerical simulation was set at 1×10^{-4} for momentum and continuity equations.

To evaluate the computational accuracy of the UMI simulation and the ordinary simulation, a space-averaged error norm of a variable, a (velocity vector, $\mathbf{u}$, or pressure, p), in a monitoring domain Ω was defined by the following equation:

$$\bar{e}_\Omega(a,t) = \frac{1}{N} \sum_{X_n \in \Omega} \left| \frac{a_{cn}(t) - a_{sn}(t)}{a_{\text{ref}}} \right|, \tag{14}$$

where n and N are the identification number and the total number of the monitoring points, respectively, $|\cdot|$ is the absolute value for scalar variables or the l_1 norm, $|u| + |v| + |w|$, for velocity vector $\mathbf{u}$, and a_{ref} is the characteristic value for normalization: $a_{\text{ref}} = U$ for velocity or $a_{\text{ref}} = \rho U^2$

for pressure. Subscripts, c and s, means UMI simulation or ordinary simulation and the standard solution, respectively.

3.2. Results and discussion

The results of the UMI simulation with/without pressure compensation were evaluated by error norms of the velocity vector and pressure in feedback domain M (or the aneurysmal domain), $\bar{e}_M(\mathbf{u}, t)$ and $\bar{e}_M(p, t)$, and compared with those of the ordinary numerical simulation. The variations of $\bar{e}_M(\mathbf{u}, t)$ and $\bar{e}_M(p, t)$ of the UMI simulations at $K_v^* = 0$, 80 and 160 are shown in Figure 3. The UMI simulations diverge at $K_v^* \geq 170$ in the case of $\Delta t = 0.01$ as revealed in our previous study [22]. There is an inversely proportional relationship between the time increment and the maximum feedback gain. Concerning this issue, we theoretically clarified that the feedback signal in the source term destabilized the iterative calculation, and proposed a computational scheme to remove the destabilization phenomenon [32]. However, we used the previous scheme in this study because improvement of computational accuracy of pressure can be discussed in a stable region with the feedback gain of $K_v^* < 170$. In the case of $K_v^* = 0$, which corresponds to the ordinary simulation without feedback, neither error norm temporally changes because the steady solution was set as the initial condition (a dotted line in Figure 3). In contrast, by applying feedback in the UMI simulations at $K_v^* = 80$ and 160, the error norm of the velocity vector, $\bar{e}_M(\mathbf{u}, t)$, monotonically decreases and converges at each constant value (dashed and solid black lines in Figure 3(a)). This indicates that the velocity field of the UMI simulation is closer to the standard solution than that of the ordinary
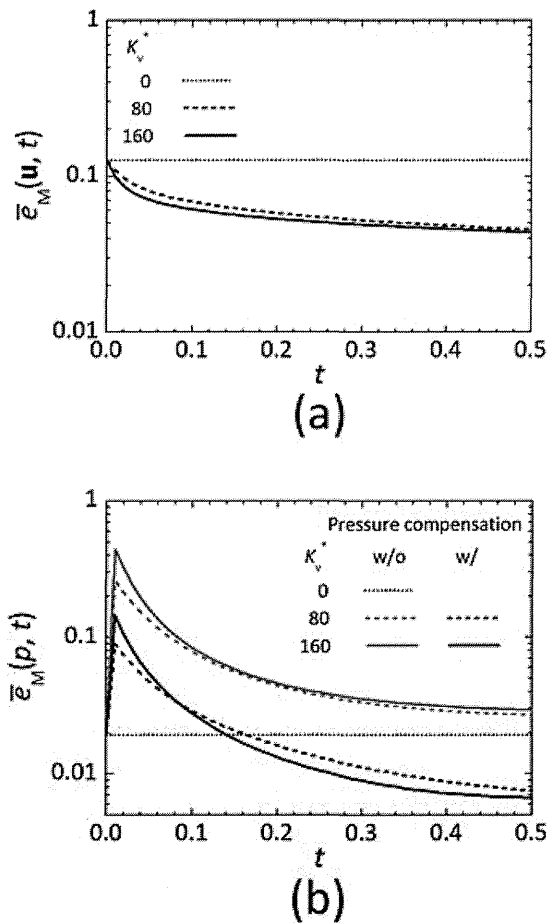

Figure 3. Transient changes of space-averaged error norms of (a) velocity vector and (b) pressure in the feedback domain in the UMI simulations without/with pressure compensation at $K_v^* = 0$, 80, and 160 (nondimensional).

simulation. Moreover, the larger feedback gain reduces the error more rapidly. On the other hand, the error norm of pressure, $\bar{e}_M(p, t)$, of the UMI simulations without pressure compensation drastically increases at the first time step ($t = 0.01$), and then decreases toward each constant value (dashed and solid gray lines in Figure 3(b)). With either feedback gain, the convergent value of $\bar{e}_M(p, t)$ remains larger than that of the ordinary simulation, indicating deterioration of the computational accuracy of the pressure field by the feedback. Generally, improvement of the computational accuracy of the velocity field leads to better reproduction of the pressure field as time progresses. However, as described in the theoretical analysis, pressure error against the standard solution arises because the feedback signals do not become zero so as to reduce the error derived from a constant difference of the boundary conditions. The results of $\bar{e}_M(p, t)$ by the UMI simulations at $K_v^* = 80$ and 160 with pressure compensation are presented with dashed and solid black lines in Figure 3(b), respectively. In the time of $t > 0.2$, the error norms of the pressure of the UMI simulations are smaller than that of the ordinary simulation. This means that the pressure field approaches the standard solution, cancelling the error in the pressure field caused by feedback signals. Moreover, the UMI simulation with a large feedback gain $\left(K_v^* = 160\right)$ presents a larger value of $\bar{e}_M(p, t)$ than that of the UMI simulation with a small feedback gain $\left(K_v^* = 80\right)$ at the beginning of the computation, but it finally gives a smaller convergent value.

The variations of steady values of the space-averaged error norms of the velocity vector and pressure in the feedback domain M, $\bar{e}_M(\mathbf{u}, t_\infty)$ and $\bar{e}_M(p, t_\infty)$ ($t_\infty = 20$), with the feedback gain are shown in Figure 4. In the UMI simulation, the value of $\bar{e}_M(\mathbf{u}, t_\infty)$ monotonically decreases
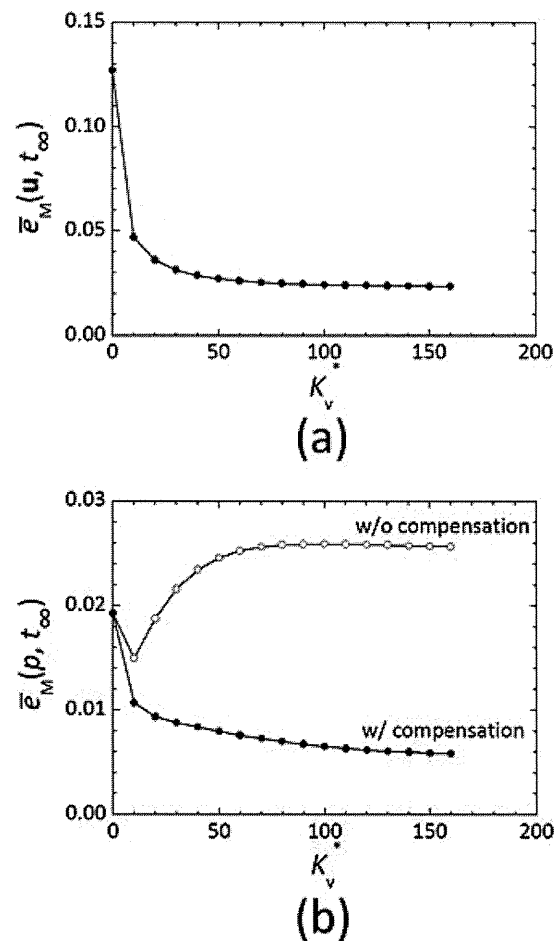

Figure 4. Variations of steady values of space-averaged error norms of (a) velocity vector and (b) pressure in the feedback domain with feedback gain (nondimensional).

with increasing feedback gain (Figure 4(a)). Note that the error norm of the velocity vector in the UMI simulation is not affected by the pressure compensation. However, the value of $\bar{e}_M(p,\ t_\infty)$ at first decreases and then increases (open circle plots in Figure 4(b)). In $K_v^* > 20$, the error norm is larger than that of the ordinary simulation $\left(K_v^* = 0\right)$. When the feedback gain is relatively small $\left(K_v^* < 20\right)$, the computational accuracy of the pressure field seems to be improved in accordance with the improvement of that of the velocity field because the pressure deviation as a result of the application of artificial body forces (or feedback signals) is not significant. With large feedback gain, however, the ability to reproduce the pressure field deteriorates because the significant artificial body forces proportional to the feedback gain are applied. In contrast, as the feedback gain increases, the value of $\bar{e}_M(p,\ t_\infty)$ after the pressure compensation monotonically decreases, similar to that of the velocity vectors (solid circle plots in Figure 4(b)). This reflects the fact that the pressure field concurrently becomes closer to the standard solution with the velocity field. Regarding the determination of the feedback gain, K_v^*, in the practical application of the UMI simulation, although the UMI simulation with a large feedback gain reduces the error against the measurement data, it reproduces the measurement error as well. In our previous study [23], the effects of major measurement errors on the computational accuracy of the UMI simulation were investigated, and methods to compensate those effects were proposed. An appropriate value of the feedback gain should be determined based on the results, considering how much compensation is achieved. It is also noted that the UMI simulation has sufficiently high frequency response characteristics to ensure the convergence to the unsteady flow [22].

The result of the UMI simulation at $K_v^* = 160$ is further investigated in the following. The steady values of the space-averaged error norms of velocity vector and pressure against the standard solution in each z-directional cross-section, $\bar{e}_{cs(z)}(\mathbf{u},\ t_\infty)$ and $\bar{e}_{cs(z)}(p,\ t_\infty)$ ($t_\infty = 20$), in the ordinary simulation $\left(K_v^* = 0\right)$ and the UMI simulations without/with the pressure compensation are shown in Figure 5(a) and (b), respectively. The dotted line and the gray and black solid lines represent the results of the ordinary simulation and the UMI simulations without and with the pressure compensation, respectively, and the gray area indicates the feedback domain in the UMI simulation. Compared with the ordinary simulation, in the case of the UMI simulations, the error norm of the velocity vector, $\bar{e}_{cs(z)}(\mathbf{u},\ t_\infty)$, is decreased after the feedback domain ($z \geqslant 1.193$), and remains smaller in a certain downstream region of the feedback domain ($2.897 < z < 3.8$), as shown by the solid lines in Figure 5(a). Regarding the error norm of pressure, $\bar{e}_{cs(z)}(p,\ t_\infty)$, shown in Figure 5(b), the UMI simulation with the pressure compensation presented a smaller value than the ordinary simulation in all z-directional cross-sections and almost the same value near the downstream boundary, implying the ability to reproduce the pressure field with good accuracy. On the other hand, the error norm of pressure, $\bar{e}_{cs(z)}(p,\ t_\infty)$, in the UMI simulation without pressure compensation increases in the upstream region of the feedback domain and exceeds that of the ordinary simulation with the peak value near the upstream boundary of the feedback domain. It then decreases in the downstream direction and becomes the same as that in the UMI simulation with the pressure compensation. Figure 5(c) shows a summation of absolute values of the divergence of the feedback force vector in each z-directional cross-section. The value is large in the upstream side in the feedback domain where the error in the velocity field is large, especially at the upstream boundary of the feedback domain where feedback signals discontinuously change. Moreover, in comparison with Figure 5(b), the large value of the divergence of the feedback force vector also influences the computational accuracy of the pressure field in the upstream domain before the feedback domain where the divergence is zero.

The pressure distributions on a y-directional cross-section ($y = 1.462$) of the standard solution, the ordinary simulation $\left(K_v^* = 0\right)$, and the UMI simulations $\left(K_v^* = 160\right)$ without/with the pressure compensation are depicted in Figure 6. Between the pressure fields of the standard solution and the ordinary simulation, p_s and p_o (Figures 6(a) and (b)), a difference can be observed near the upstream boundary, but similar pressure profiles are obtained in the aneurysm. As observed in the error norm of pressure in Figure 5(b), the UMI simulation without pressure compensation (Figure 6(c)) provides a pressure distribution different from that of the standard solution (Figure 6(a)), especially in the upstream region of the feedback domain (see an arrow), but it gives almost the same distribution in the aneurysm. In the UMI simulation with the pressure compensation (Figure 6(d)),
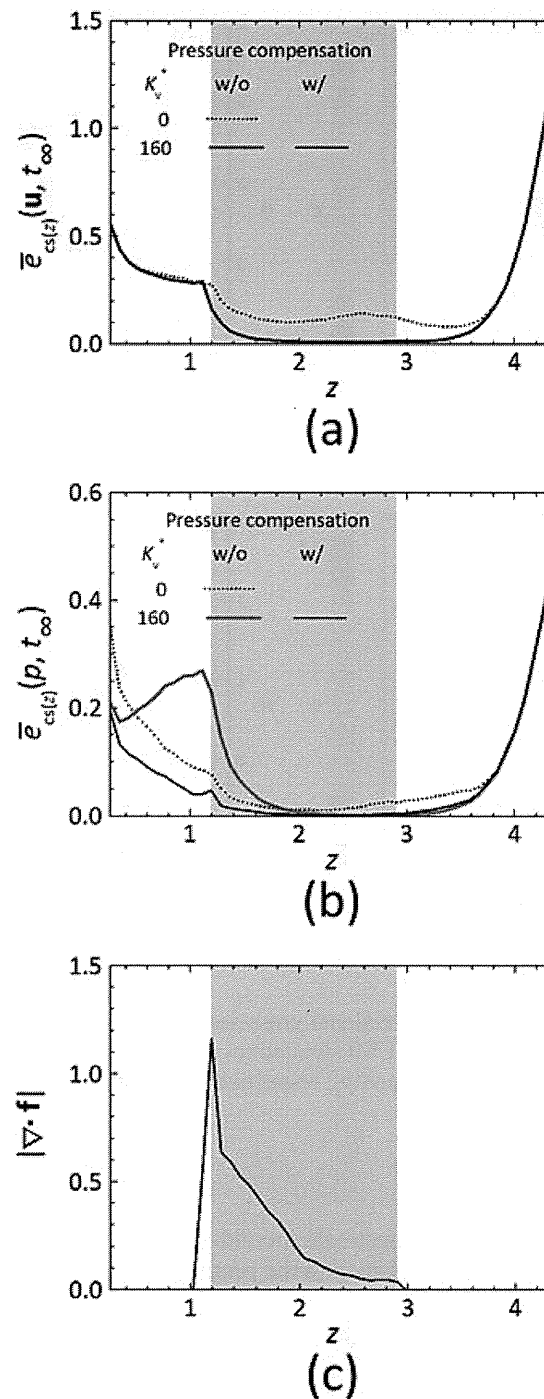
Figure 5. Steady values of space-averaged error norms of (a) velocity vector and (b) pressure, and (c) space-averaged absolute value of divergence of feedback signal vector in each z-directional cross-section (nondimensional). The gray zone implies the feedback domain.

the difference in pressure distribution observed in the UMI simulation without the pressure compensation is properly improved.

The distributions of error norm of pressure against the standard solution on the corresponding y-directional cross-section are shown in Figure 7. As mentioned above, the ordinary simulation and the UMI simulation without the pressure compensation show relatively large error near the upstream